**Proceedings of ASME Turbo Expo 2021**
**Turbomachinery Technical Conference and Exposition**
**GT2021**
**June 7-11, 2021, Virtual, Online**

**GT2021-59851**

# AN EXPERIMENTAL INVESTIGATION INTO THE IMPACTS OF VARYING THE CIRCUMFERENTIAL EXTENT OF TIP-LOW TOTAL PRESSURE DISTORTION ON FAN STABILITY

**Oliver Allen*, Alejandro Castillo Pardo, Cesare A. Hall**
Whittle Laboratory
University of Cambridge
1 JJ Thomson Avenue
Cambridge CB3 0DY, UK

## ABSTRACT

*Future jet engines with shorter and thinner intakes present a greater risk of intake separation. This leads to a complex tip-low total pressure distortion pattern of varying circumferential extent. In this paper, an experimental study has been completed to determine the impact of such distortion patterns on the operating range and stalling behaviour of a low-speed fan rig. Unsteady casing static pressure measurements have been made during stall events in 11 circumferential extents of tip-low distortion. The performance has been measured and detailed area traverses have been performed at rotor inlet and outlet in 3 of these cases - clean, axisymmetric tip-low and half-annulus tip-low distortion. Axisymmetric tip-low distortion is found to reduce stall margin by 8%. It does not change the stalling mechanism compared to clean inflow. In both cases, high incidence at the tip combined with growth of the casing boundary layer drive instability. In contrast, half-annulus tip-low distortion is found to reduce stall margin by only 4% through a different mechanism. The distortion causes disturbances in the measured casing pressure signals to grow circumferentially in regions of high incidence. Stall occurs when these disturbances do not decay fully in the undistorted region. As the extent of the distorted sector is increased, the stability margin is found to reduce continuously. However, the maximum disturbance size before stall inception is found to occur at intermediate values of distorted sector extent. This corresponds to distortion patterns that provide sufficient circumferential length of undistorted region for disturbances to decay fully before they return to the distorted sector. It is found that as the extent of the tip-low distortion sector is increased, the circumferential size of the stall cell that develops is reduced. However, its speed is found to remain approximately constant at 50% of the rotor blade speed.*

## INTRODUCTION

Future turbofan engine designs aim to increase propulsive efficiency by reducing the fan pressure ratio and increasing the bypass ratio [1,2]. This leads to larger diameter fans. To alleviate the detrimental increase in engine weight and drag, shorter and thinner intakes are installed. At off-design conditions, such as crosswind and high angle of attack, intake separation may occur. Thus, the fan could experience complex tip-low total pressure inflow distortion patterns of varying circumferential extent [3]. NASA tests in the 1970s demonstrated that radial tip-low total pressure distortion reduces the stability margin and causes a radial flow redistribution [4]. Prior work on the impact of varying the circumferential extent of distortion has focused on quantifying its impact on fan performance and stability margin [5,6].

Compressor stall has been studied extensively in recent history [7]. The most common stall mechanism in aero-engines, including in the rig considered in this paper is the spike-type stall. It originates from the growth and propagation of small length

*Current affiliation: Rolls-Royce plc., PO Box. 3, Filton, Bristol BS34 7QE, United Kingdom (oliver.allen@rolls-royce.com)

scale disturbances [8, 9]. Both axisymmetric and circumferentially varying inlet distortion are known to reduce stability margin. Analytical attempts to model this, using well-known parallel compressor [10, 11] and alternative methods [6, 12], typically overpredicted the reduction in stability margin. More recent experimental and computational studies have shown that circumferentially varying distortion causes a three-dimensional flow redistribution upstream of the fan [13–15]. An experimental study on stall in a low-speed, boundary layer ingesting (BLI) fan rig was recently completed [16]. In this study, unsteady casing pressure measurements were used to link the growth in amplitude of large pressure fluctuations to regions of high local incidence in a circumferentially varying inflow distortion pattern. Stall was found to occur when these disturbances became sufficiently large that they did not decay in the undistorted region. However, the precise link between the circumferential extent of tip-low distortion, the growth of unsteady pressure fluctuations and fan stability remains poorly understood.

This paper aims to experimentally determine the impact of tip-low total pressure distortion patterns of varying circumferential extent on the operating range and stalling behaviour of a low-speed fan. Although the use of a low speed fan does not permit compressible flow effects to be characterised, it allows detailed measurements to be taken without significantly changing the flow-field. The approach taken considers three inflows in detail: clean, radial tip-low distorted and half-annulus tip-low distorted. Although these patterns are simplified compared to the inflow distortion generated by intake separations, they are useful to isolate the key impacts of axisymmetric and circumferentially varying tip-low total pressure distortion on the steady and unsteady aerodynamics of the fan.

Radial and full annulus traverses were used to resolve the steady flow-field upstream and downstream of the rotor at near stall operating points in each case. Unsteady casing pressure measurements were then used to determine the differences in the development of spike-type disturbances around stall inception in each case. From these measurements, the effects of axisymmetric and a circumferentially varying tip-low inflow distortion were analysed. Unsteady pressure measurements around stall inception were completed for a further 8 circumferential extents of tip-low distortion ($\Lambda$). These were used to analyse the effect of varying $\Lambda$ on the maximum spike-type disturbance size observed at the last stable operating point. For all values of $\Lambda$ tested, Kiel probe rakes were used to measure constant speed characteristic lines, and estimate the change in stability margin and rotor pressure rise.

It is shown that increasing the circumferential extent of tip-low inflow distortion ($\Lambda$) reduces the stall margin and rotor total to static pressure rise coefficient. In all cases tested, stall inception is linked to regions of high incidence and casing boundary layer separation. Circumferentially varying tip-low distortion is shown to change the stalling mechanism to one in which disturbances (regions of instability) grow and decay as they move around the annulus. Furthermore, the fan is shown to remain stable despite the presence of large disturbances at intermediate extents of tip-low distortion ($120^\circ < \Lambda < 280^\circ$). The fan is shown to be stabilised by undistorted regions, where the incidence and radial extent of casing boundary layer separation are reduced, and the disturbances decay. Stall is only found to occur when the disturbances reach a sufficient size that they do not fully decay in the undistorted region.

## EXPERIMENTAL METHODS

The experimental rig used for this study is a low-speed single-stage fan, known as the BLI rig. This rig was originally commissioned for the analysis of low hub-to-tip radii ratio BLI fan aerodynamics [14–17]. This facility was recently updated for the analysis of aft-section BLI fuselage fan aerodynamics [18]. The experiments described in this paper were conducted in the latter configuration, which is characterised by the design point parameters presented in Table 1.

Figure 1(a) depicts the meridional view of the BLI fan rig. The rig has a long intake duct which enables the free interaction of the rotor blades with the incoming distorted flow. The annulus geometry resembles the CENTRELINE aft-section fuselage fan [19]. Figure 2 presents three sections of the rotor blades used in this study. These blades were designed for a continuous and severe hub total pressure distortion [18]. A mid-span loaded work profile along with controlled leading edge alignment was chosen to improve the blade distortion tolerance. The low-speed nature of the rig does not allow full-scale compressibility effects to be replicated. However, the velocity triangles of the full-scale transonic fuselage fan [20] are reproduced by matching the full-scale flow coefficient and stage loading coefficient presented in Table 1. A variable circumferential extent ($\Lambda$), defined in Fig. 1(b), of tip-low distortion could be generated with a set of distortion gauzes.

**TABLE 1: Design point parameters for the BLI fan rig.**

| | |
|---|---|
| Flow coefficient $\phi$ | 0.69 |
| Stage loading coefficient $\Psi_{tt}$ | 0.44 |
| Rotor inlet tip Mach number | 0.16 |
| Rotor tip Reynolds number | $2.1 \cdot 10^5$ |
| Rotor hub-to-tip radii ratio | 0.51 |
| Running tip clearance (% span) | 0.35 |
| Number of rotor, OGV blades | 20, 30 |

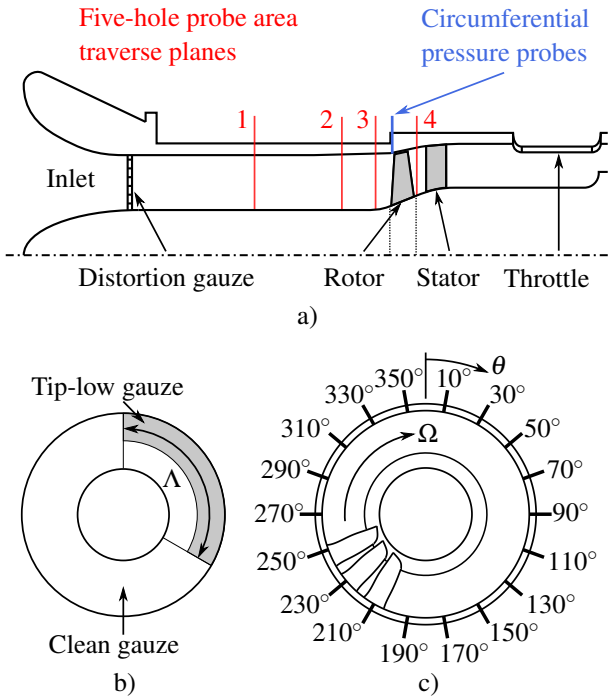


**FIGURE 1: Experimental setup: a) Meridional view of the BLI fan rig indicating locations of measurement stations b) Distortion gauze sketch indicating the distortion extent, c) Schematic of the location of unsteady pressure transducers.**

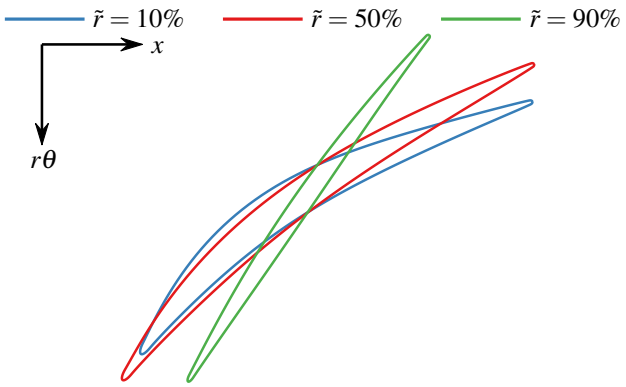


**FIGURE 2: Rotor blade sections.**

Steady-state measurements were used to resolve the time-averaged flow-field at the rig inlet, rotor inlet and rotor outlet planes. They were carried out using a five-hole pneumatic probe mounted on an area traverse system at measuring stations 1, 3 and 4, respectively. The diameter of the head of the probe was 2.0% of the rotor inlet span. The probe measured the time-averaged values of stagnation pressure, static pressure, swirl angle and radial flow angle. The uncertainties of probe measurements were of the order of $\pm 0.5\%$ and $\pm 1.0\%$ of the dynamic head for the stagnation and static pressure fields; and of the order of $\pm 0.5^\circ$ for flow angles. For clean and tip-low axisymmetric inflows the traverse was reduced to radial, with 21 endwall clustered radial positions. However, full annulus area traverses were required for non-axisymmetric inflows. For these measurements, the traverse system operated in a $36^\circ$ sector with 29 endwall clustered radial positions and 37 equally spaced circumferential positions. Rotating the distortion gauze ten times relative to this sector enabled the measurement of the full annulus flow field. Station 1 is equipped with 6 rakes of Kiel probes equally spaced in the circumferential direction. Each rake comprises 5 probes clustered radially to measure equal area. The rakes are used along with standard hub and casing static pressure taps to estimate the overall performance of the fan.

Fast response pressure probe transducers were used to measure unsteady casing static pressure fluctuations around the annulus. A total of 18 equally spaced pressure probes were flush mounted in the casing at a plane 10% of axial chord upstream of the rotor leading edge. The circumferential position of each pressure transducer is presented in Fig. 1(c) in terms of the angle $\theta$. The signal was sampled at $50 f_{bp}$ and low-pass filtered to reduce noise. The filter, characterised by a cutoff frequency of $16.7 f_{bp}$, was applied at the amplifier. The sampling frequency was sufficiently higher than the Nyquist frequency to avoid aliasing. An additional once-per-revolution signal generated by an optical sensor was acquired at the same sampling frequency to track the position and speed of the rotor shaft.

Flow conditioning gauzes were installed at the intake of the rig to generate different inlet flow patterns. Each gauze comprises a large number of small-scale circumferential and radial vanes with precisely controlled geometry. These were designed using the method proposed in [21] and additively manufactured as a single thick sheet. The full annulus gauze was composed of 10 independent $36^\circ$ annular sector gauzes. Each of these sectors could be a *clean* or *tip-low* gauze, shown in Figs. 3(a) and 3(b). The clean gauze was designed to provide an axial uniform flow across the span. The tip-low distortion gauze was designed to match the clean gauze below 60% span and to produce the highest feasible stagnation pressure drop above 80% span. The resulting axial velocity profiles, as measured at station 1 for axisymmetric inflow conditions at near stall, are presented in Fig 3(c). The circumferential extent of the distortion $\Lambda$ could be varied by adjusting the number of tip-low gauze sectors included in the annulus.

## Unsteady Data Analysis

Spectral analysis was used to investigate the frequency content of the pressure signals at different times and locations. The key measure used here was the energy spectral density $S(f)$ of a

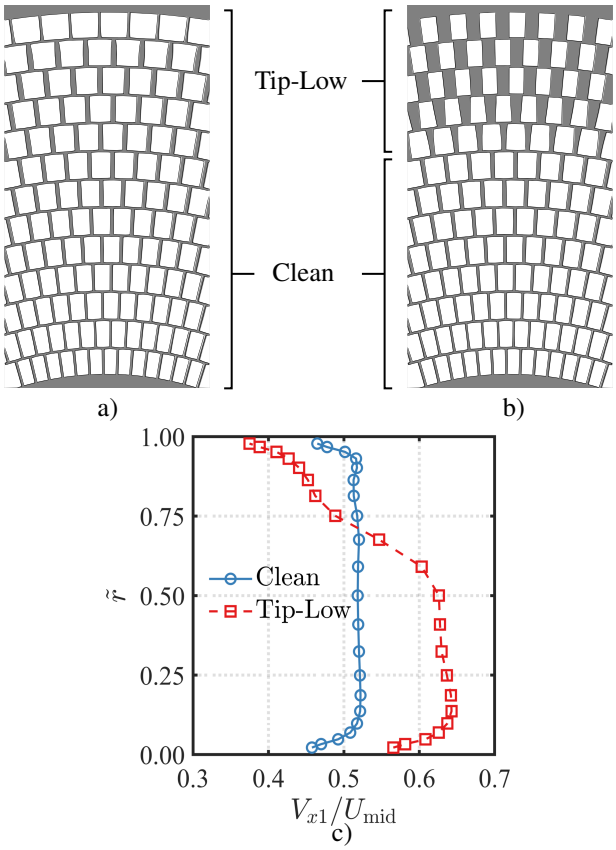


**FIGURE 3: Flow conditioning gauzes, a) Clean, b) Tip-low distortion, c) Radial profiles**

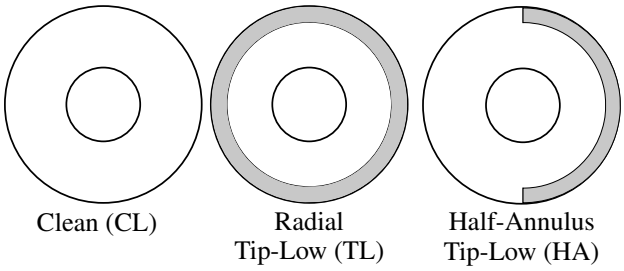


**FIGURE 4: Schematics of key distortion cases tested**

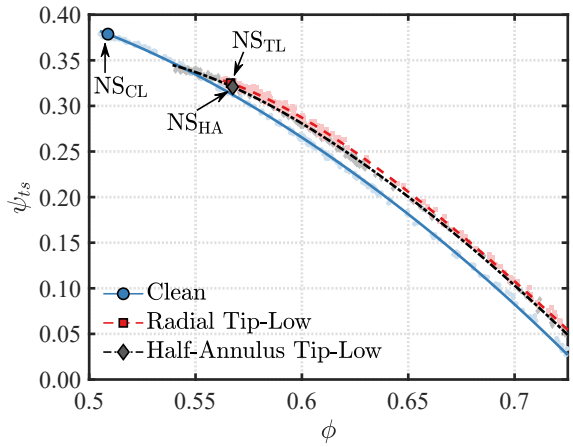


**FIGURE 5: Measured constant speed characteristic lines**

signal $p(t)$, which was found from the magnitude of the Fourier transform, i.e.

$$S(f) = \left| \int_{-\infty}^{\infty} p(t) e^{-2\pi i f t} dt \right|^2 \tag{1}$$

This was used to determine the energy content of each frequency in a signal. It was also used to evaluate the fraction of the total energy contained within the frequency range $f_1 < f < f_2$,

$$\frac{\Delta E}{E} = \frac{\int_{f_1}^{f_2} S(f) df}{\int_0^{\frac{1}{2} f_s} S(f) df} \tag{2}$$

The measured pressure signal of a given probe $p$ can be split into its time average component $\bar{p}$ and the unsteady fluctuation $p'$, i.e., $p = \bar{p} + p'$. The average magnitude of the fluctuation can be quantified using the standard deviation, given by

$$\sigma = \sqrt{\overline{(p-\bar{p})^2}} = \sqrt{\overline{p'^2}} \tag{3}$$

## Distortion Cases Tested

Steady flow-field measurements were completed for three inlet flow conditions to the fan:

1. *Clean* (CL): uniform axial flow.
2. *Radial tip-low* (TL): axisymmetric deficit of total pressure near the tip.
3. *Half annulus tip-low* (HA): $180^o$ of total pressure deficit near the tip, uniform flow elsewhere ($\Lambda = 180^\circ$).

Figure 4 shows these cases schematically. Figure 5 shows constant speed characteristic lines for these cases in terms of the rotor inlet flow coefficient and total-to-static pressure rise coefficient across the rotor ($\psi_{ts}$). These were calculated using the Kiel probe rakes. At the indicated near stall (NS) operating points, steady-state area traverses were completed. The point $\text{NS}_{\text{HA}}$ is further from the stall point in this case to maintain stability while a full-annulus area traverse was completed over a long time period. Constant speed characteristic lines were measured for a further 8 circumferential extents of tip-low distortion to locate the stall point (ST), and determine the stall margin, defined as the percentage change in flow coefficient between the design and stall point (Fig. 6). The different extents were created by varying

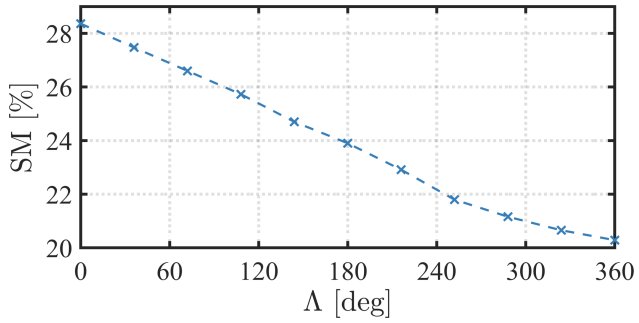


**FIGURE 6: Variation of stall margin with circumferential extent of tip low distortion**

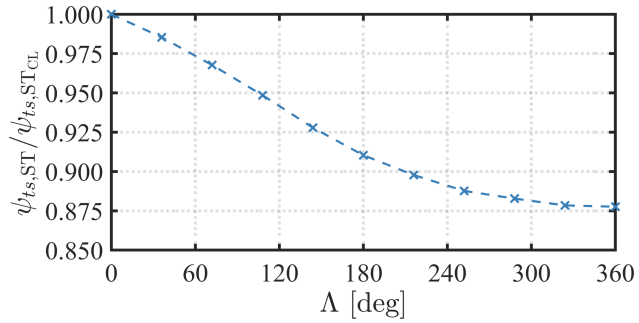


**FIGURE 7: Variation of maximum total to static pressure rise coefficient with circumferential extent of tip low distortion**

the number of 36° tip-low gauze sectors. Increasing the distorted sector extent consistently reduces the stall margin. Axisymmetric tip-low distortion reduces the stall margin by 8%. Half annulus tip-low reduces the stall margin by 4%. Increasing the distorted sector extent also consistently reduces the rotor total to static pressure rise coefficient (Fig. 7). Axisymmetric tip-low distortion reduces it by 12%. Half-annulus tip-low distortion reduces it by 9%. The rate of decrease is greatest at intermediate distorted sector extent ($45° < \Lambda < 200°$). At high distorted sector extent ($\Lambda > 240°$), the rate of decrease reduces significantly.

## EFFECT OF AXISYMMETRIC TIP-LOW DISTORTION

### Steady Flow-Field Near Design Flow Coefficient

The impact of axisymmetric tip-low distortion on the mass flow distribution at near design point flow coefficient is presented in Fig. 8(a). Upstream of the fan, reduced axial momentum is observed in the distorted region. To keep the same flow coefficient as the clean case, the deficit of axial velocity found above 70% span is balanced by an excess of axial velocity below the same span section. The reduced axial velocity near the tip is linked to reduced total pressure in the distorted region. Thus, the radial flow migration towards the casing that takes places upstream

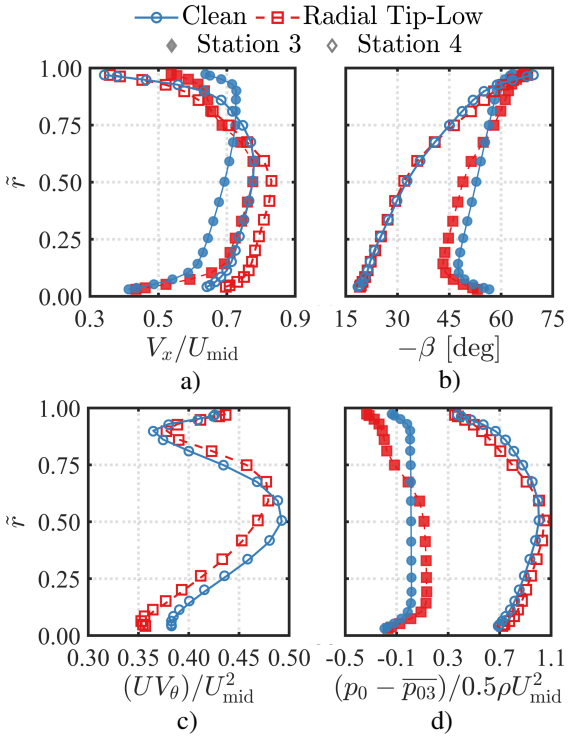


**FIGURE 8: Rotor radial flow profiles near design point, a) axial velocity, b) relative swirl angle, c) outlet specific angular momentum, d) total pressure**

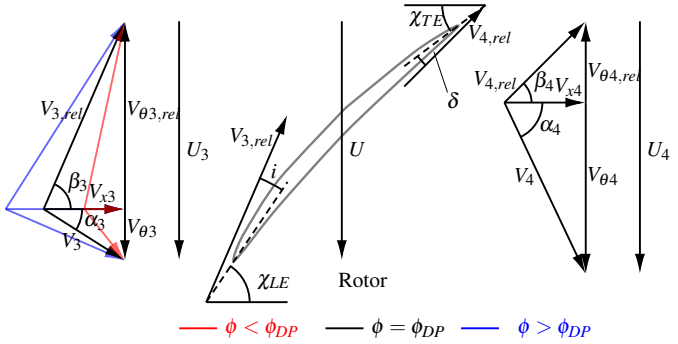


**FIGURE 9: Rotor blade velocity triangle changes due to stagnation pressure distortion.**

and across the fan is intensified. The ultimate effect is the homogenisation of the axial velocity profile at the rotor outlet (Fig. 8(a)). This intensified radial flow redistribution in radial inflow distortion has been reported in previous studies [4, 18].

The rotor blade incidence distribution, shown in terms of the inlet relative swirl angle (Fig. 8(b)) is primarily driven by the axial velocity distribution in each case (Fig. 9), as the inlet absolute swirl angle in each case is small. In the distorted case,

the tip operates in a region with reduced axial velocity. Thus, the incidence there is increased. Despite the off-design incidence, the blade deviation remains fairly constant across the span. This is shown in Fig. 8(b) in terms of the outlet relative swirl angle.

The non-dimensional version of the Euler work equation is given by

$$\frac{\Delta h_0}{U_{\text{mid}}^2} = \frac{U_3^2}{U_{\text{mid}}^2}\left(\frac{U_4^2}{U_3^2} + \frac{U_4}{U_3}\frac{V_{x4}}{V_{x3}}\frac{V_{x3}}{U_3}\tan\beta_4 - \frac{V_{x3}}{U_3}\tan\alpha_3\right) \quad (4)$$

For this type of distortion the dominant term is the local flow coefficient $V_{x3}/U_3$. The velocity deficit found in the tip-low distorted region results in increased loading (as $\beta_4 < 0$). The rest of the blade operates at a higher flow coefficient, leading to reduced blade loading. In the absence of absolute inlet swirl, the specific outlet angular momentum is equivalent to the non-dimensional work defined in Eq. (4). Thus, the changes in loading are reflected by the specific outlet angular momentum distribution (Fig. 8(c)). The design intent mid-span loaded work distribution can also be seen in both cases. The extra work applied to the flow in the upper part of the span results in higher pressure rise across the rotor (Fig. 8(d)). This balances the deficit of total pressure caused by the distortion. Reduced pressure rise takes place elsewhere. Overall, tip-low distortion leads to a consistent increase in pressure rise coefficient along the characteristic line (Fig. 5).

## Unsteady Measurements During a Stall Event

To measure the unsteady pressure fluctuations during stall events, the rig was initially started near design conditions. The throttle was then closed gradually until stall took place. The measured pressure traces were low pass filtered at $0.9f_{bp}$ to remove the dominant blade passing frequency component.

Figure 10 compares the pressure traces from two flow conditions: clean and axisymmetric tip-low distortion. The traces are almost identical in both cases. There are small fluctuations from -10 revs. Larger spikes develop from $t \approx 0$. These spikes travel around the annulus and grow rapidly in magnitude to form a rotating stall cell. The stall cell's angular extent is reduced by 40° in the distorted inflow, but its speed does not change. This is unexpected as numerous previous studies have found that larger stall cells rotate more slowly. In both cases, a single stall cell rotating at about $0.5\Omega$ was observed.

Spectrograms of a single casing pressure trace for both cases are shown in Figure 11. In both cases, prior to stall, all the spectral energy is contained in the blade passing frequency and its harmonics. There is a clear change in frequency content at the stall point. The blade passing frequency and its harmonics always have the highest energy. After stall, the frequency content at all other frequencies increases significantly.

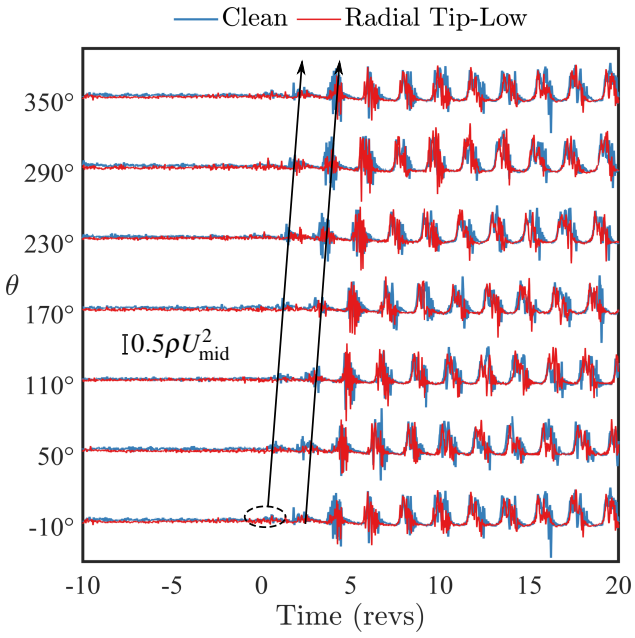


**FIGURE 10: Filtered unsteady casing pressure traces during a stall event in clean and radial tip-low distorted inflow**

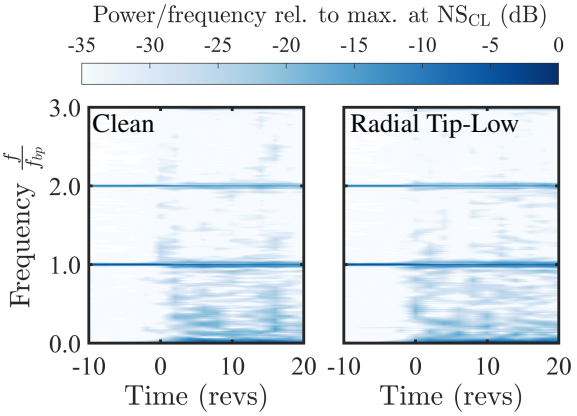


**FIGURE 11: Spectrograms of the casing pressure signals at $\theta = 350°$ in clean and radial tip-low distorted inflows during a stall event**

## Linking the Steady Flow-Field to Stalling Behaviour

To further characterise the stall behaviour under different axisymmetric inflows, the onset of stall is linked to the steady flow-field at the near stall operating point. In both cases, a sudden change in frequency content is observed at the stall point (Fig. 11). This is associated with a rapid disturbance development. Regions of high incidence levels have been previously linked to disturbance growth [16]. The operation at a reduced flow coefficient results in increased incidence levels across the span, with

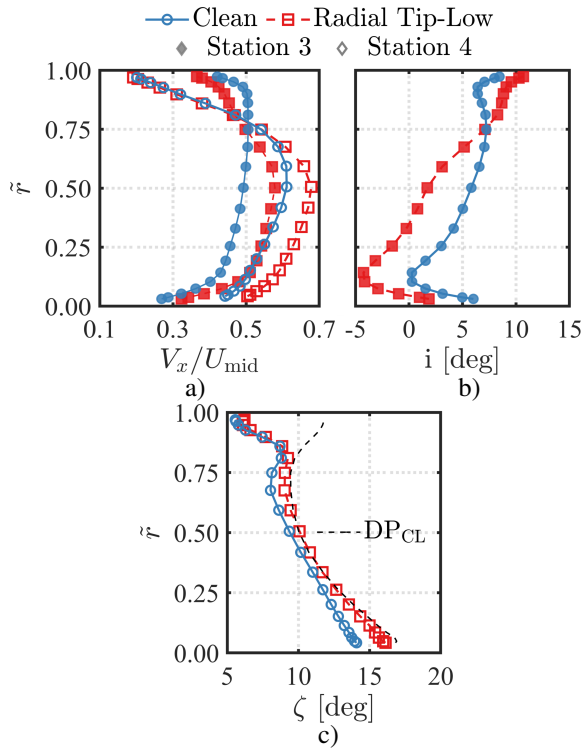


**FIGURE 12: Rotor radial flow profiles near stall, a) axial velocity, b) incidence onto blades, c) radial flow angle**

the highest values located in both cases near the tip (Fig. 12(b)). The velocity deficit associated with the distorted region, shown in Fig. 12(a), leads to a further increase in incidence (Fig. 12(b)). However, the fan is able to operate stably with these increased levels of incidence. Thus, the high levels of incidence at the tip section alone did not drive the onset of stall.

Figure 12(c) compares the spanwise distributions of outlet radial flow angle near stall with the corresponding clean distribution at near design. Below 75% span no significant difference is observed between near design and near stall. However, in the upper part of the span, a reduction in tipwards flow is observed near stall. This can be associated with the growth of the casing boundary layer within the rotor blade passages. The increasing casing blockage was confirmed by CFD simulations.

The growth and separation of the casing boundary layer caused a partial blockage of the rotor blade passages near the tip. At the last stable operating point, the rotor outlet axial velocity profiles overlap above 75% (Fig. 12(a)). Despite the different inlet axial velocity, the outlet properties in this region ($\tilde{r} > 75\%$) are highly similar. This suggests that the radial extent of the casing boundary layer blockage is similar for both cases. Thus, stall inception in tip-low distortions is also linked to the radial extent of the rotor blade passage blockage at clean near stall. Therefore, stall was driven by a combination of high rotor tip incidence and the blade passage blockage associated with casing boundary layer separation. Distortion was found to increase the incidence near the tip and produce an earlier onset of the casing boundary layer separation, reducing stall margin by $\approx 8\%$.

## EFFECT OF HALF-ANNULUS TIP-LOW DISTORTION

### Unsteady Measurements During a Stall Event

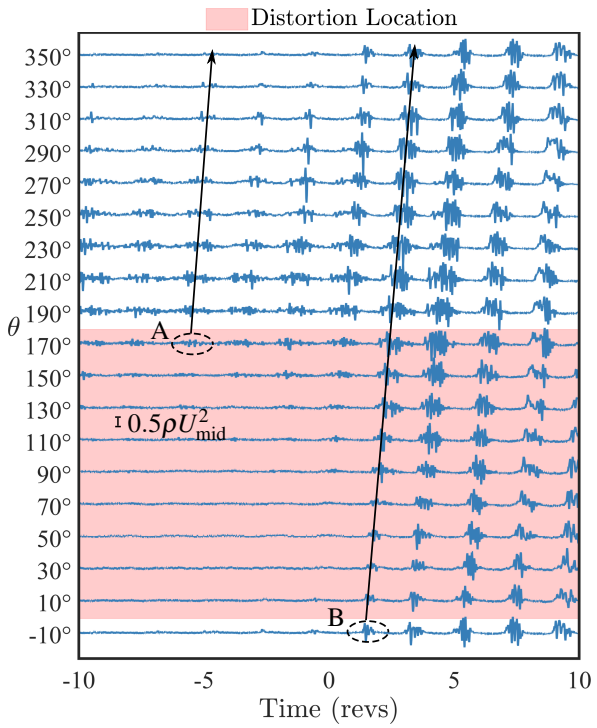


**FIGURE 13: Measured, filtered unsteady casing pressure traces during a stall event in half-annulus tip-low distortion**

Figure 13 shows the measured, low-pass filtered unsteady casing pressure traces from all 18 transducers during a stall event in half-annulus tip-low distortion. Note that in this and subsequent figures, the location of tip-low total pressure distortion is shown by a red shaded area. At A, a small disturbance develops in the tip-low sector. As it moves across the undistorted sector it decays. By the time it reaches $\theta = 350°$, it has almost completely disappeared. As the disturbance travels across the distorted sector it grows again, being visible at around $\theta = 170°$. This growth and decay cycle repeats as the throttle area was further reduced. At B, the size of the disturbance is enough that it does not fully decay before growth begins again in the distorted sector. Over each revolution, this cycle continues, promoting growth until a rotating stall cell develops. The fully developed stall cell wave-

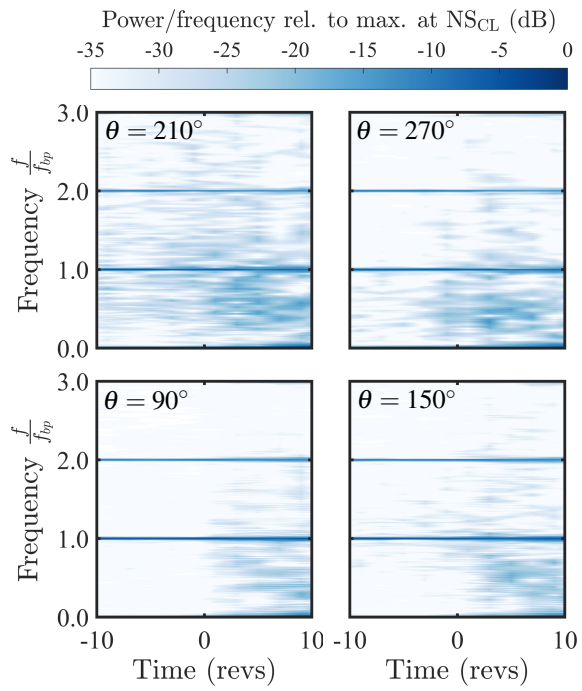


**FIGURE 14: Spectrograms of casing pressure signals at 4 circumferential locations during a stall event in half-annulus tip-low distortion**

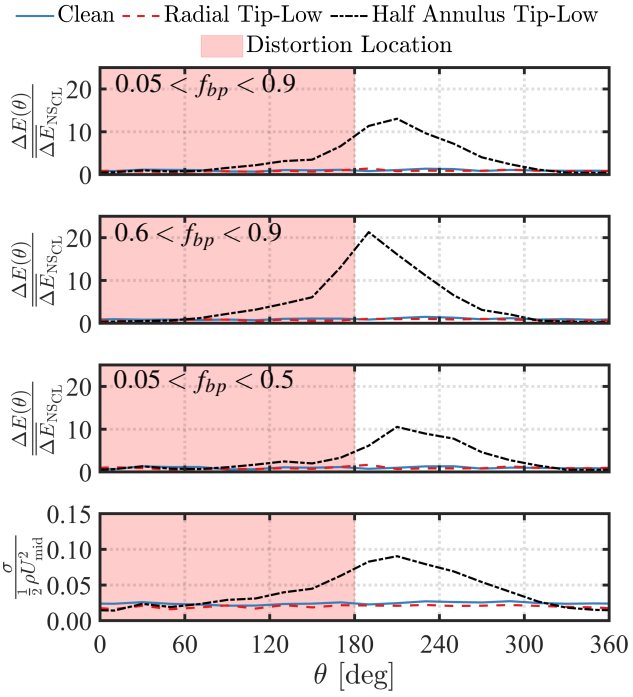


**FIGURE 15: Circumferential variation of casing pressure signal properties at the last stable operating point**

form is similar to that of the stall cell in both clean and axisymmetric tip-low distorted inflows.

Figure 14 shows the measured frequency content at 4 circumferential locations around stall inception. Prior to the stall, coming out of the distortion ($\theta = 210°$), disturbances with all frequency content are present before stall occurs. By $\theta = 270°$ most of the disturbances are at low frequencies ($f < 0.5 f_{bp}$). At $\theta = 90°$ almost no disturbances are visible. At the end of the distorted sector ($\theta = 150°$), high frequency ($0.6 f_{bp} < f < f_{bp}$) disturbances are observed before the stall point. After the stall point, all positions exhibit similar frequency content driven by the large rotating stall cell.

Two types of disturbance develop: long length-scale and short length-scale disturbances. The circumferential variation in amplitude of each type was estimated by calculating the energy content of the signal in each relevant frequency range (Eq. (2)). Frequencies below $0.05 f_{bp}$ were excluded to avoid d.c. effects. Frequencies above $0.9 f_{bp}$ were excluded to eliminate the blade passing frequency. Figure 15 shows the results of this analysis.

The fractions of energy in each frequency range in both clean inflow and axisymmetric tip-low distortion are approximately equal. This is consistent with the spectrograms, where minimal disturbances were observed before the first spike appeared and stall occurred (Fig. 11). In half-annulus tip-low distortion, disturbance growth across all frequencies starts at $\theta = 50°$ until the disturbance magnitude reaches a maximum at $190° < \theta < 230°$. Disturbances decay to below the NS$_{CL}$ level by $\theta = 320°$. The standard deviation of the signals (Eq. (3)), which is an alternative measurement of the energy of disturbances of all frequencies, shows a similar evolution. Short length scale disturbances are observed to grow and decay faster than long length scale disturbances. This is consistent with the spectrograms at $\theta = 150°$ and $\theta = 270°$ (Figure 14), where mostly short and long length scale disturbances respectively are observed.

## Linking the 3D Flow-Field to Stalling Behaviour

Half-annulus tip-low distortion creates a circumferentially varying steady flow-field. It creates 2 distinct regions of different rotor inlet axial velocity profiles - an undistorted sector (left) and a distorted sector (right) (Fig. 16(a)). This is linked to a change in stalling mechanism compared to the axisymmetric cases.

Regions of high incidence onto the fan blades are linked to stall inception, as in the axisymmetric cases. Figure 17 shows the circumferential variation of the local flow properties at 85% span section. At this location, there is a step change in axial velocity from approximately $0.48 U_{mid}$ in the distorted sector to $0.58 U_{mid}$ in the undistorted sector (Fig. 17(a)). The local incidence onto the rotor blades is driven by the axial velocity and absolute swirl angle via the inlet velocity triangles (Fig. 9). The increased incidence in the distortion is primarily driven by the reduction in axial velocity in the distorted sector (Fig. 17(c)).

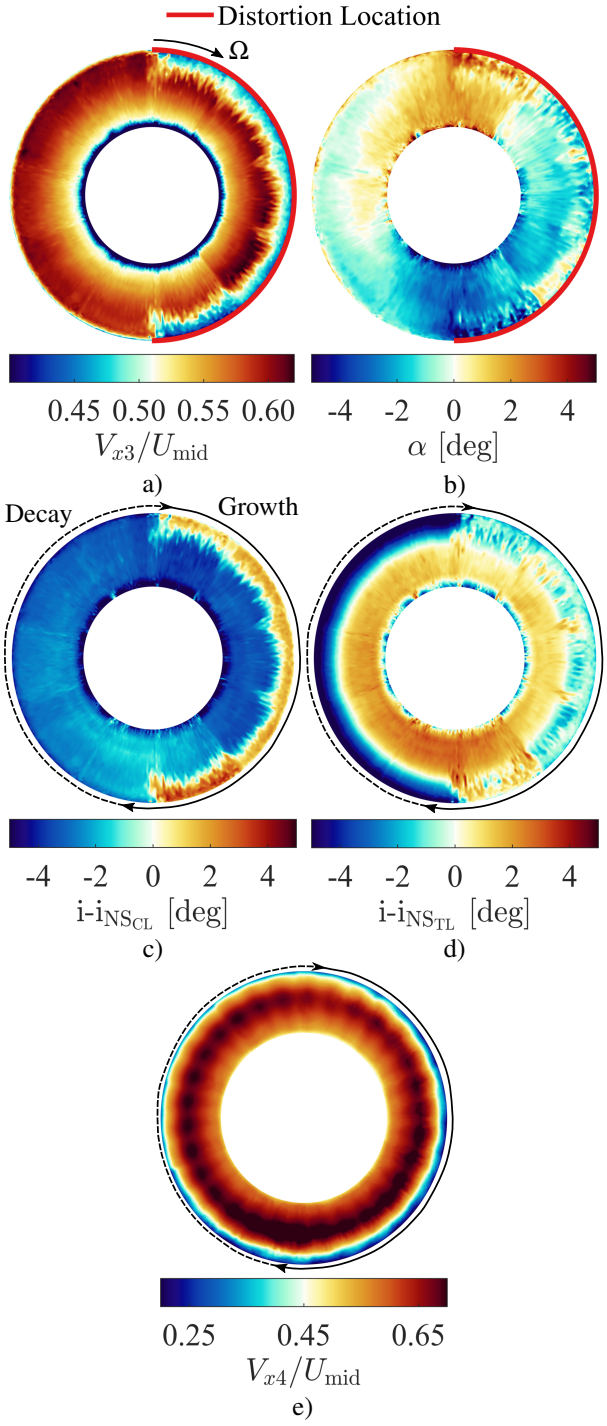


**FIGURE 16: Rotor steady flow-field at $NS_{HA}$ - a) inlet axial velocity, b) inlet swirl angle, c) incidence relative to mean level at $NS_{CL}$, d) incidence relative to mean level at $NS_{TL}$, e) outlet axial velocity**

Thus, the resulting incidence distribution is almost uniform and below the $NS_{CL}$ level, except in the distorted region, where it is locally increased (Fig. 16(c)). The measured operating point $NS_{HA}$ is further from instability than $NS_{CL}$. Thus, at the last stable operating point in half-annulus tip-low distortion the incidence is expected to increase further above the $NS_{CL}$ level in the distorted region. Disturbances grow in the distorted sector and decay in the undistorted sector (Fig. 17(e)). Thus, high incidence onto the fan blades is linked to the growth of disturbances, which were previously associated with stall inception. However, in the undistorted sector, the incidence is below the $NS_{CL}$ level, which is linked to disturbance decay, promoting stability. Hence, stall did not occur immediately after large disturbances appeared in half-annulus tip-low distortion, unlike in the axisymmetric cases.

The circumferential variation in inlet swirl angle also affects the disturbance growth and decay pattern. The distortion location is associated with a region of low static pressure. Consequently, the flow migrates radially and circumferentially from regions of high pressure (undistorted) to areas of low pressure (distorted). This flow migration creates regions of co-swirl ($\alpha > 0$) and counter-swirl ($\alpha < 0$) entering and leaving the distorted sector respectively (Fig. 16(b)). The disturbance growth rate is highest between $\theta = 110°$ and $\theta = 190°$, where the local incidence is highest. There, counter-swirl created by the flow redistribution increases the local incidence above the $NS_{TL}$ level in the distorted sector (Fig. 17(b)-(c)). The disturbance growth rate is lowest between $\theta = 10°$ and $\theta = 70°$. There, co-swirl reduces the local incidence marginally, but not below the level at $NS_{CL}$. It does reduce the incidence below the level at $NS_{TL}$. Thus, the observed circumferential flow redistribution also affects the growth and decay rates of disturbances prior to stall inception.

The increased radial extent of casing boundary layer separation is also linked to stall in half-annulus tip-low distortion, as observed in the axisymmetric cases. Between $\theta = 10°$ and $\theta = 200°$, the rotor outlet axial velocity at 85% span reduces by $0.1U_{mid}$. This is due to the radial extent of the casing boundary layer separation increasing gradually in the distorted sector, creating a partial blockage of the rotor blade passages (Fig. 16(e)). Between $\theta = 200°$ and $\theta = 250°$, this axial velocity increases rapidly, caused by a rapid decrease in the extent of casing boundary layer separation. Furthermore, it is lowest for $125° < \theta < 205°$. Noting that the full annulus mass flow averaged circumferential particle displacement $\Delta\theta = 15°$, this region corresponds to the location of the maximum disturbance growth rate. Disturbance growth also continues after incidence is reduced below the $NS_{CL}$ level at $\theta = 180°$, where the radial extent of casing separation remains high. Disturbances decay more slowly between $\theta = 210°$ and $\theta = 280°$, where incidence is reduced but the radial extent of separated flow remains high. Thus, the circumferential variation in casing boundary layer thickness and separation is linked to the growth and decay of disturbances prior to stall inception.

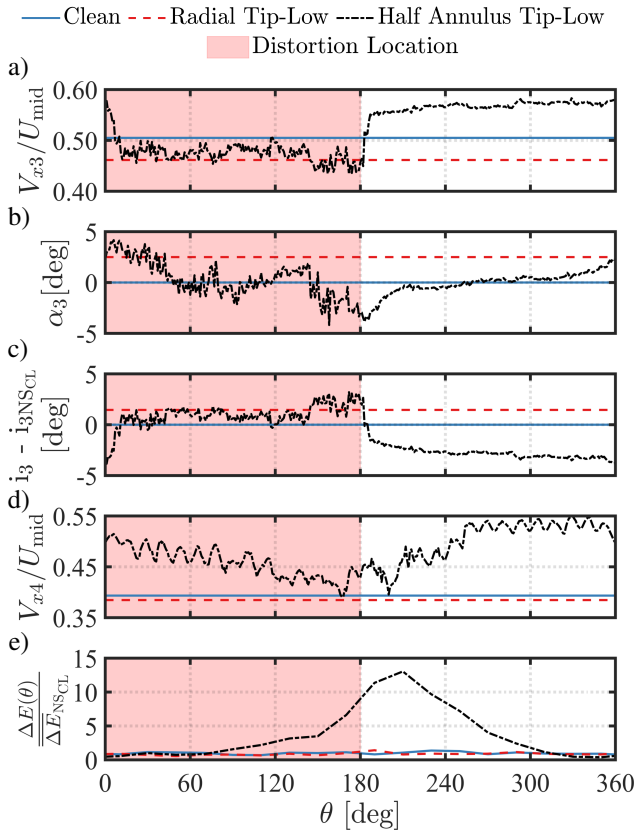


**FIGURE 17: Circumferential variation of rotor flow-field at 85% span at $\text{NS}_{\text{HA}}$ - a) inlet axial velocity, b) inlet absolute swirl, c) incidence onto rotor blades, d) outlet axial velocity, e) energy of casing pressure signals in range $0.05f_{bp} < f < 0.9f_{bp}$**

The above suggests that the initiation and growth of disturbances in regions of low momentum fluid is driven by a combination of high tip incidence (Fig. 16(c)-(d)) and partial blockages of the rotor blade passages caused by casing boundary layer separations (Fig. 16(e)). Unlike in the axisymmetric cases, stall only occurs in half-annulus tip-low distortion when these disturbances grow sufficiently large that they do not decay fully in the undistorted sector. Following this, the disturbances grow with each revolution around the annulus to form a rotating stall cell. Thus, half annulus tip-low distortion does not change the factors driving stall but does change the stall inception mechanism.

## EFFECT OF VARYING THE DISTORTED SECTOR EXTENT ON STABILITY

Unsteady casing pressure measurements were made during stall events in tip-low distortion of 8 additional values of $\Lambda$ between 0° and 360° in 36° increments. The circumferential variation of disturbance energy was quantified using the same method as in the previous cases. Only the energy variation across all disturbance frequencies ($0.05f_{bp} < f < 0.9f_{bp}$) was considered in this section, as this was related to the steady flow-field for $\Lambda = 180°$. For $\Lambda = 36°, 72°, 180°, 288°, 324°$ the results of this analysis are presented in Fig. 18.

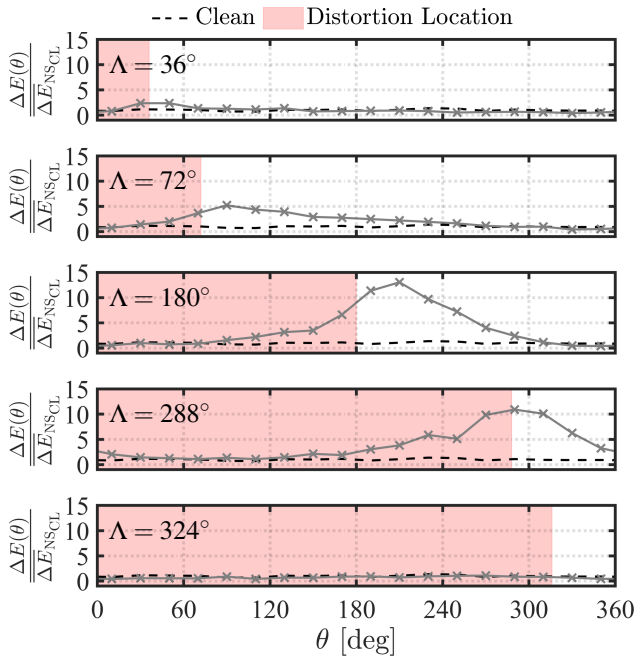


**FIGURE 18: Circumferential energy variation of casing pressure signals relative to $\text{NS}_{\text{CL}}$ level at the last stable operating point in frequency range $0.05f_{bp} < f < 0.9f_{bp}$**

Disturbances grow in distorted regions and decay in undistorted regions, as discussed for the half-annulus tip-low case. Comparing $\Lambda = 36°$ and $\Lambda = 72°$ shows that increasing the size of the distorted sector increases the proportion of the annulus over which disturbances develop, increasing their maximum magnitude. These disturbances decay fully in the undistorted sector. For $\Lambda = 180°$, large disturbances develop in the distorted sector and decay in the undistorted sector. Comparing $\Lambda = 288°$ and $\Lambda = 324°$ shows that reducing the size of the undistorted sector at high $\Lambda$ reduces the proportion of the annulus over which disturbances decay, reducing the maximum disturbance magnitude that is observed prior to instability occurring.

Thus, two factors drive the variation of maximum disturbance size with $\Lambda$ (Fig. 19). When the distorted sector size is small ($\Lambda < 120°$), only small disturbances can grow at the last stable operating point. As the distorted sector size is increased to $120° < \Lambda < 280°$, the largest possible disturbances grow. However, the fan is stabilised by the undistorted sector, so these large

disturbances do not lead to the immediate onset of instability. For $\Lambda > 280°$, the undistorted sector is too small to reduce the disturbance size sufficiently to prevent instability occurring.

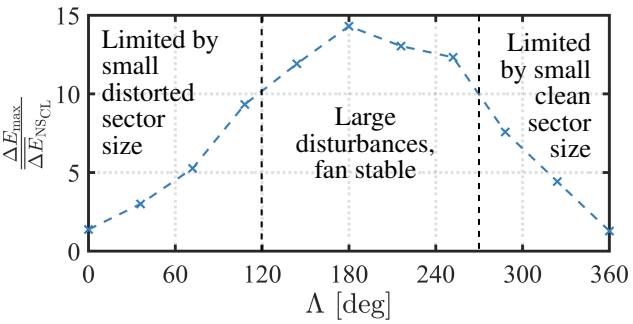


**FIGURE 19: Variation of maximum energy of casing pressure signals in range $0.05f_{bp} < f < 0.9f_{bp}$ at last stable operating point with Λ**

The rotational speed and circumferential size of the fully developed stall cell were estimated for each value of Λ tested. Figure 20 illustrates the method used to estimate the circumferential extent. As the circumferential extent of tip-low distortion increases, the size of the fully developed stall cell decreases (Fig. 21(a)), but its speed does not change, remaining at approximately $0.5\Omega$ (Fig. 21(b)). Numerous previous studies have found that larger stall cells rotate more slowly, however this was not observed here. The overall area of the stall cell may not change significantly between cases because it is also affected by the radial extent of the blockage, which could not be determined. In this study, therefore, the stall cell speed may not be expected to change as its circumferential extent reduces.

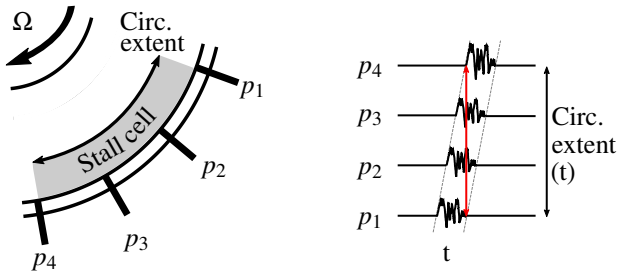


**FIGURE 20: Illustration of method used to estimate circumferential extent of stall cell**

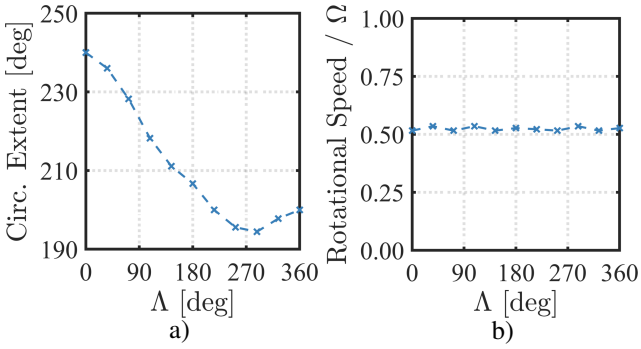


**FIGURE 21: Variation of stall cell properties with Λ a) circumferential extent, b) angular speed**

## CONCLUSIONS

1. The stalling behaviour of a low-speed fan rig has been experimentally tested in clean inflow and tip-low total pressure distortion of varying circumferential extent
2. Increasing the circumferential extent of tip-low distortion (Λ) was found to reduce the stability margin and rotor total to static pressure rise coefficient. Axisymmetric tip-low distortion reduced stability margin by 8% and the pressure rise coefficient by 12% relative to clean inflow. Half-annulus tip-low distortion reduced stability margin by around 4% and the pressure rise coefficient by 9%.
3. Axisymmetric tip-low distortion was not found to change the stall inception mechanism. Stall was found to be driven by a combination of high tip incidence onto the rotor blades and the separated casing boundary layer causing partial blockages of the rotor blade passages.
4. Half annulus tip-low distortion was found to change the stalling mechanism. Large disturbances in the casing pressure signals were found to grow in the distorted sector, in regions of high tip incidence and casing boundary layer separation. These disturbances were found to decay in the undistorted sector. Stall occurred when the disturbances became sufficiently large that they did not decay fully in the undistorted sector enabling a rotating stall cell to develop.
5. When the circumferential extent of distortion (Λ) was varied, the maximum disturbance amplitude at the last stable operating point was found to be driven by 2 factors. At low Λ, the small size of the distorted sector was found to limit the size of disturbances that grew. At high Λ, the small size of the undistorted sector was found to limit the area over which disturbances decayed, so instability occurred almost immediately. The fan remained stable despite the presence of large disturbances at intermediate Λ, as they decayed fully in the undistorted region.

## ACKNOWLEDGMENT

The authors are grateful to the EU project CENTRELINE, grant agreement ID 723242, for the use of their rotor. At the Whittle Laboratory, James Taylor is thanked for his technical advice setting up the rig. Elliot Reed and Josh Firman are also thanked for their technical support manufacturing and assembling the rig.

## NOMENCLATURE

### Symbols

E Energy
f Frequency
h Enthalpy
i Incidence angle
p Pressure
r Radius, radial coordinate
S Energy spectral density
SM Stall margin = $(\phi_{DP} - \phi_{NS})/\phi_{DP}$
t Time
U Rotor blade speed
V Velocity
$\alpha$ Absolute swirl angle
$\beta$ Relative swirl angle
$\zeta$ Radial flow angle
$\theta$ Circumferential coordinate
$\Lambda$ Circumferential extent of tip-low distortion
$\rho$ Air density
$\sigma$ Standard deviation
$\Omega$ Shaft angular velocity

### Abbreviations

BLI Boundary layer ingesting
DP Near design operating point
NS Near stall operating point
ST Stall point (last stable operating point)
revs Rotor revolutions

### Non-dimensional Groups

$\phi$ Flow coefficient = $\dot{m}/\rho A U_{mid}$
$\Psi_{tt}$ Stage loading coefficient = $\Delta h_0/U_{mid}^2$
$\psi_{ts}$ Rotor pressure rise coefficient = $(p_4 - p_{01})/0.5\rho U_{mid}^2$

### Subscripts

*bp* Blade passing
CL Clean inflow
HA Half-annulus tip-low distorted inflow
mid Value at midspan
TL Radial tip-low distorted inflow
*ts* Total to static
*tt* Total to total
*x* Axial coordinate
0 Stagnation quantity
1 Value just downstream of gauze (station 1)
3 Value at rotor inlet (station 3)
4 Value at rotor outlet (station 4)

## REFERENCES

[1] Hughes, C., Zante, D. V., and Heidmann, J., 2013. Aircraft Engine Technology for Green Aviation to Reduce Fuel Burn. Technical Memorandum TM—2013-217690, National Aeronautics and Space Administration.

[2] Peters, A., Spakovszky, Z. S., Lord, W. K., and Rose, B., 2014. "Ultrashort Nacelles for Low Fan Pressure Ratio Propulsors". *Journal of Turbomachinery,* ***137***(2), p. 021001.

[3] Freeman, C., and Rowe, A. L., 1999. "Intake Engine Interactions of a Modern Large Turbofan Engine". In Proceedings of the ASME 1999 International Gas Turbine and Aeroengine Congress and Exhibition, no. 99-GT-344, American Society of Mechanical Engineers.

[4] Sandercock, D. M., and Sanger, N. L., 1974. "Some Observations of the Effects of Radial Distortions on Performance of a Transonic Rotating Blade Row". Technical Note NASA TN D-7824, National Aeronautics and Space Administration.

[5] Reid, C., 1969. "The Response of Axial Flow Compressors to Intake Flow Distortion". In Proceedings of the ASME 1969 Gas Turbine Conference and Products Show, no. 69-GT-29, American Society of Mechanical Engineers.

[6] Hynes, T. P., and Greitzer, E. M., 1987. "A Method for Assessing Effects of Circumferential Flow Distortion on Compressor Stability". *Journal of Turbomachinery,* ***109***(3), pp. 371–379.

[7] Day, I. J., 2015. "Stall, Surge, and 75 Years of Research". *Journal of Turbomachinery,* ***138***(1), p. 011001.

[8] Day, I. J., 1993. "Stall Inception in Axial Flow Compressors". *Journal of Turbomachinery,* ***115***(1), pp. 1–9.

[9] Weichert, S., and Day, I., 2013. "Detailed Measurements of Spike Formation in an Axial Compressor". *Journal of Turbomachinery,* ***136***(5), p. 051006.

[10] Pearson, H., and McKenzie, A. B., 1959. "Wakes in Axial Compressors". *The Journal of the Royal Aeronautical Society,* ***63***(583), p. 415–416.

[11] Mazzawy, R. S., 1977. "Multiple Segment Parallel Compressor Model for Circumferential Flow Distortion". *Journal of Engineering for Power,* ***99***(2), pp. 288–296.

[12] Longley, J. P., 1990. "Measured and Predicted Effects of Inlet Distortion on Axial Compressors". In Proceedings of the ASME 1990 International Gas Turbine and Aeroengine

Congress and Exposition, no. 90-GT-214, American Society of Mechanical Engineers.
[13] Jerez Fidalgo, V., Hall, C. A., and Colin, Y., 2012. "A Study of Fan-Distortion Interaction Within the NASA Rotor 67 Transonic Stage". *Journal of Turbomachinery,* ***134***(5), p. 051011.
[14] Gunn, E. J., Tooze, S. E., Hall, C. A., and Colin, Y., 2013. "An Experimental Study of Loss Sources in a Fan Operating with Continuous Inlet Stagnation Pressure Distortion". *Journal of Turbomachinery,* ***135***(5), p. 051002.
[15] Gunn, E. J., and Hall, C. A., 2014. "Aerodynamics of Boundary Layer Ingesting Fans". In Proceedings of the ASME Turbo Expo 2014, no. GT2014-26142, American Society of Mechanical Engineers.
[16] Perovic, D., Hall, C. A., and Gunn, E. J., 2019. "Stall Inception in a Boundary Layer Ingesting Fan". *Journal of Turbomachinery,* ***141***(9), p. 091007.
[17] Gunn, E. J., and Hall, C. A., 2017. "Non-Axisymmetric Stator Design for Boundary Layer Ingesting Fans". In Proceedings of the ASME Turbo Expo 2017, no. GT2017-63082, American Society of Mechanical Engineers.
[18] Castillo Pardo, A., and Hall, C. A., 2019. "Aerodynamics of Boundary Layer Ingesting Fuselage Fans". In Proceedings of the 24th ISABE Conference, no. ISABE-2019-24162, International Society of Air Breathing Engines.
[19] Seitz, A., Habermann, A. L., Peter, F., Troeltsch, F., Castillo Pardo, A., Della Corte, B., van Sluis, M., Goraj, Z., Kowalski, M., Zhao, X., Grönstedt, T., Bijewitz, J., and Wortmann, G., 2021. "Proof of Concept Study for Fuselage Boundary Layer Ingesting Propulsion". *Aerospace,* ***8***(1).
[20] Castillo Pardo, A., and Hall, C. A., 2020. "Design of a Transonic Boundary Layer Ingesting Fuselage Fan". In Proceedings of GPPS Chania20, no. GPPS-CH-2020-0042, Global Power and Propulsion Society.
[21] Taylor, J. V., 2019. "Complete Flow Conditioning Gauzes". *Experiments in Fluids,* ***60***(3), p. 35.